31st Congress of the International Council
of the Aeronautical Sciences

Belo Horizonte, Brazil; September 09-14, 2018

AERODYNAMIC AND AEROACOUSTIC INVESTIGATION OF SWIRL RECOVERY VANES FOR PROPELLER PROPULSION SYSTEMS

Luc E. van den Ende, Qingxi Li, Francesco Avallone, Damiano Casalino, Georg Eitelberg,
Leo L.M. Veldhuis
Delft University of Technology, Kluyverweg 1, 2629 HS, Delft, the Netherlands

Keywords: *Swirl recovery vanes, propellers, LBM, slipstream, unsteady flow, noise*

Abstract

Swirl recovery vanes (SRVs) are effective in increasing the propulsive efficiency of propeller propulsion systems. Due to the highly periodic flow in the propeller slipstream, unsteady phenomena emerge on the vanes. As the design process omits these phenomena, this manuscript quantifies their relevance and their effect on the far-field noise. Simulations with a lattice-Boltzmann method have been carried out for the aerodynamic flow field, while the far-field noise is computed using the Ffowcs Williams-Hawkings integral solution. The impingement of the propeller blade wake and of the propeller tip vortices on the vanes cause peaks in the thrust generated by the vanes. It is found that the installation of the SRVs causes tonal noise at harmonics of the blade passage frequency, which increases the overall sound pressure both in the upstream and downstream directions. The first harmonic produced by the propeller blades is found to be dominant in the region of maximum noise where the vanes have a minimal contribution.

1 Introduction

Renewed interest in turboprop engines exists for their high propulsive efficiency. This efficiency can be further increased by exploiting the swirl energy present in the slipstream of propellers, for example using swirl recovery vanes (SRVs).

Careful design of the SRVs is required in order to increase the propulsive efficiency [1, 2]. Since the SRVs are exposed to highly turbulent and unsteady flow which is neglected in the design process, it is interesting to delve deeper into the unsteady effects with the aim of improving the design.

Besides the benefit of providing extra thrust, the SRVs may also generate additional noise due to the unsteady loading and impingement of propeller tip vortices. Acoustic measurements performed by NASA [3] show no additional noise production by the SRVs. On the other hand, it is observed in Ref. [4] that the sound pressure level increases by 2 to 6 dB compared to the isolated propeller when the SRVs are installed. Taking into account that both experiments were performed at distinct flow conditions using different geometry, the discrepancy may be clarified by a computational campaign. The CFD software PowerFLOW based on a lattice Boltzmann method (LBM) coupled with a very large eddy simulation (VLES) turbulence model will be adopted.

The manuscript is organized such that the geometry is presented first in Sec. 2. Following, the methodology is described in Sec. 3 including the main numerical method and the methods used for validation. The grid refinement study and the validation are included in Sec. 4 and 5 before getting to the results in Sec. 6. The main findings of the work are summarized in the conclusive section.

2 Geometry

The adopted geometry follows directly from Ref. [1] and is presented in Fig. 1 together with the adopted axis system. The propeller is a scaled model of a conventional propeller from a typical regional turboprop aircraft. It features six blades and a diameter D of 0.4064 m. The hub of the propeller is 0.084 m in diameter, the root chord c_r 33 mm in length and the blade pitch angle equals 30° at 70% of the radius R.

The SRV design framework was developed in Ref. [1] and is based on a lifting-line model combined with an airfoil design process. As a test example, a set of SRVs was designed for a freestream velocity $V_\infty = 29$ m/s at a high propeller loading condition with an advance ratio $J = 0.6$, where the advance ratio is defined as [5]:

$$J = \frac{V_\infty}{nD} \tag{1}$$

where n is the rotational velocity in revolutions per second (RPS) and D the diameter of the propeller. The vane count is set to 4 and the vanes feature the same radius as the propeller. They are positioned on a fairing of diameter $0.31D$ with their leading edge 94 mm behind the propeller. The chord at the root measures 60 mm and 40 mm at the tip. At the design condition, an extra 3.4% thrust was predicted by the lifting line method and 2.6% was measured in the experimental tests.

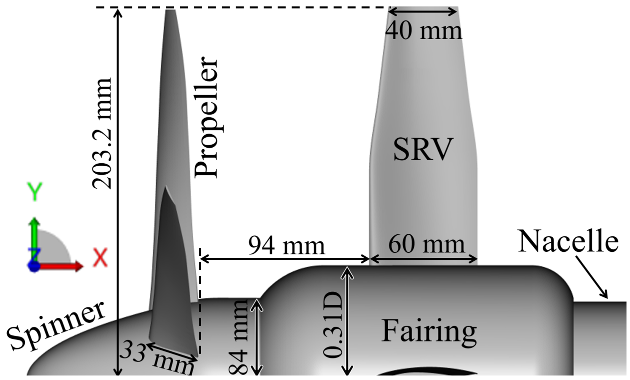

Fig. 1 : Geometry of propeller with SRVs.

3 Methodology

3.1 LBM

3.1.1 Flow solver

A lattice Boltzmann method (LBM) is chosen for this study as it is widely validated for aerodynamic and aeroacoustic simulations of rotors [6, 7, 8] and as it is inherently time-dependent [9]. The commercial software 3DS-Simulia PowerFLOW 5.4a is adopted.

LBM determines the macroscopic flow variables starting from the mesoscopic kinetic equation, i.e. the Boltzmann equation. The distribution of particles is solved on a Cartesian mesh, known as a lattice. Since an explicit time integration method is used, the Courant-Friedrichs-Lewy (CFL) stability number is set to unity by the solver to ensure stable conditions. The lattice Boltzmann equation can be written as:

$$g_i(\mathbf{x} + \mathbf{c}_i \Delta t, t + \Delta t) - g_i(\mathbf{x}, t) = C_i(\mathbf{x}, t), \tag{2}$$

where g_i is the particle distribution function along the i-th lattice direction. $\mathbf{c}_i \Delta t$ and Δt are space and time increments, respectively. $C_i(\mathbf{x}, t)$ is the collision term for which the Bhatnagar-Gross-Krook (BGK) model [10, 11] is adopted because of its simplicity:

$$C_i(\mathbf{x}, t) = -\frac{\Delta t}{\tau}\left[g_i(\mathbf{x}, t) - g_i^{\mathrm{eq}}(\mathbf{x}, t)\right], \tag{3}$$

where τ is the relaxation time and g_i^{eq} is the local equilibrium distribution function.

A very large eddy simulation (VLES) model is implemented to take into account the effect of the sub-grid unresolved scales of turbulence. Following Yakhot and Orszag [12], a two-equations $k-\varepsilon$ renormalization group (RNG) is used to compute a turbulent relaxation time that is added to the viscous relaxation time. In order to reduce the computational cost, a pressure-gradient-extended wall-model (PGE-WM) is used to approximate the no-slip boundary condition on solid walls [13, 14].

3.1.2 Noise computations

The compressible and time-dependent nature of the transient computed solution together with the low dissipation and dispersion properties of the LBM scheme [15] allow extracting the sound pressure field directly in the near-field up to a cut-off frequency corresponding to approximately 15 voxels per acoustic wavelength.

However, in the far-field, noise can be computed more efficiently through an integral extrapolation of the near-field solution based on the Ffowcs Williams-Hawkings analogy [16]. The formulation 1A, developed by Farassat and Succi [17], extended to a convective wave equation, is used in this study [15]. The formulation is implemented in the time domain using a source-time dominant algorithm [18]. Integrations are performed on the solid surfaces where the unsteady pressure is recorded on the finest mesh resolution level with a measurement frequency equal to 15 times the 12th harmonic of the blade passing frequency (BPF). As a consequence, acoustic dipoles distributed on the surfaces are the only source terms of interest [19] and the non-linear contribution related to the turbulent fluctuations in the wake of the propeller is neglected.

3.1.3 Computational setup

The simulation volume has a length of $25.7D$ and a width and height of $15D$. The center and origin are defined by the intersection of the propeller axis with the propeller plane. A velocity inlet is defined with a V_∞ of 29 m/s and a temperature of 293.15 K. The outlet is defined by a static pressure of 101,325 Pa and a free flow direction. No-slip boundary conditions are applied on the propeller, SRVs, spinner and fairing. A free-slip boundary condition is applied to the nacelle which extends to the outlet plane. A rotating reference frame is defined for the propeller and spinner with an angular velocity of 119 RPS, corresponding to the operating condition of $J = 0.6$. After reaching time convergence, i.e. two propeller rotations, results are stored for three propeller rotations.

12 variable resolution (VR) regions are defined which are numbered increasing with resolution. The regions close to the geometry are visualized in Fig. 2. The resolution increases with a factor of two from one VR region to the next. The finest region (VR12) consist of an offset of $0.030c_r$ from a region around the leading edge (LE, displayed in orange in Fig. 2), trailing edge (TE, green) and the tip (blue) of both the propeller and vanes. This is done in order to capture the high pressure gradients in these regions accurately and to have an adequate representation of the propeller tip vortex development on the SRVs. The LE and TE regions are defined to be approximately 10% of the local chord. The propeller tip region has a similar size and the vane tip region has a spanwise length of $0.16R$.

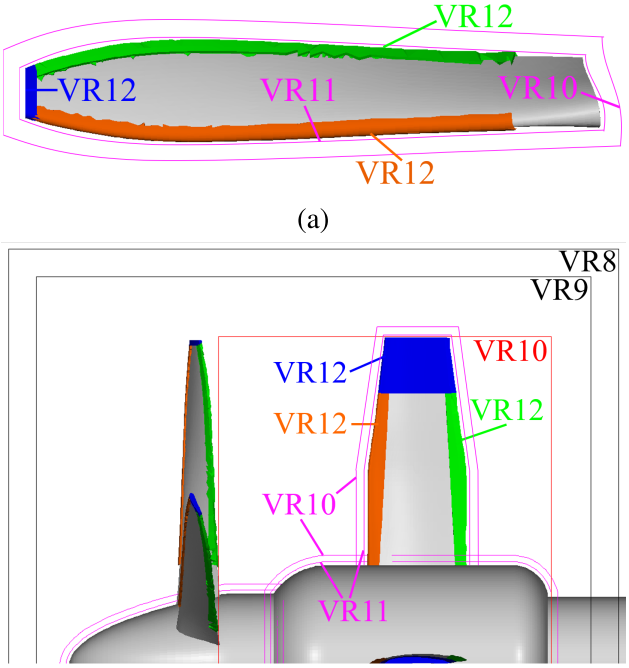

(a)

(b)

Fig. 2 : Visualization of the near-field VR regions around a propeller blade (a) and the other components (b).

VR11 and VR10 consist of regions around all no-slip boundary surfaces with offsets of respectively $0.061c_r$ and $0.18c_r$. These regions are displayed in purple in Fig. 2. Additionally, VR10 consists of a cylinder region (in red) aimed at capturing the propeller slipstream. This cylinder has a diameter of $1.0D$ and ranges from

$x = 0.45c_r$ to $x = 6.8c_r$. VR9 (in black) consists of a cylinder of diameter $1.2D$, ranging from $x = -3.0c_r$ to $x = 7.6c_r$. VR8 (also black) to VR2 are defined by and offset from this cylinder, sized such that there are 10 voxels present in between two cylinder boundaries. Finally, VR1 is the simulation volume.

3.2 RANS

A Reynolds-averaged Navier Stokes (RANS) simulation of the isolated propeller has been performed previously for which the results are used for validation purposes in the current study. A description of the method can be found in Ref. [1].

3.3 Experimental Setup

Experiments were conducted with the designed SRVs and the propeller model in a low-speed open-jet wind tunnel at Delft University of Technology. Measurements were obtained using a rotating shaft balance for the propeller, a load cell for the SRVs and particle-image velocimetry (PIV) to obtain the velocity planes that will be used for validation. The measured SRVs' thrust at the design point equals 2.6% of the propeller thrust with an uncertainty of 0.4 percentage point [1].

4 Grid Refinement Study

In order to have a grid-independent solution, a grid refinement study is performed using the isolated propeller configuration. The time-averaged propeller thrust coefficient $C_{T_{prop,avg}}$ is used as reference variable which is defined as [5]:

$$C_{T_{prop,avg}} = \frac{T_{prop,avg}}{\rho n^2 D^4} \tag{4}$$

where $T_{prop,avg}$ is the average propeller thrust, ρ the air density, n is the rotational velocity in RPS and D the diameter of the propeller.

Four different grids are generated with increasing resolution. In Fig. 3 the propeller thrust coefficients for the different grids are displayed. The resolution is expressed as voxel per physical length for the VR12 region. A clear converging trend is visible and an excellent match is obtained with the values obtained using RANS and experiment. The finest grid is herewith accepted and will be used in the remainder of this manuscript.

The convergence of aeroacoustic results is guaranteed by comparing the overall sound pressure level (OSPL) at a point at a distance $2D$ and an angle of 90° from the propeller axis, displayed in red in Fig. 3.

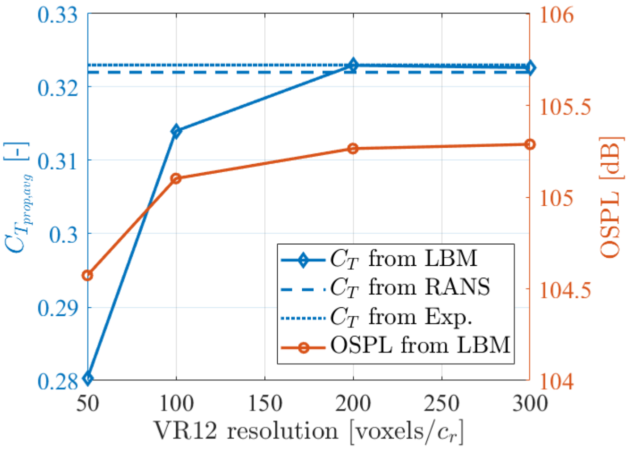

Fig. 3 : Averaged propeller thrust coefficient and OSPL at a point in the propeller plane at a distance $2D$ from the propeller axis. Obtained using grids with different resolution.

5 Validation of Propeller Slipstream

The method is further validated comparing the axial velocity V_a and tangential velocity V_t in a plane downstream of the isolated propeller. The results are time-averaged over three propeller rotations and spatially-averaged into thirty radial segments. In Fig. 4, the results are presented and compared to RANS and experimental results.

A good agreement is observed, especially for the more outboard regions. Small scale root vortices originating from the propeller are present close to the fairing. The resolution used in LBM is expected to be insufficient to capture these vortices accurately, which would be the cause of the discrepancies for $r/R < 0.5$. Further study into resolving these vortices by adding additional resolution is required.

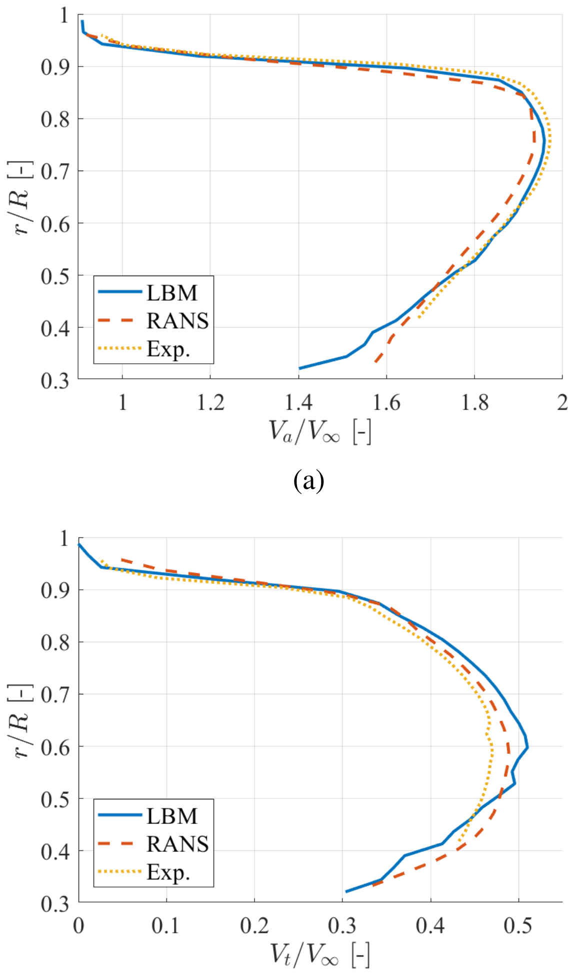

(a)

(b)

Fig. 4 : Time- and spatially-averaged axial (a) and tangential (b) velocity in a plane downstream of the propeller at $x/D = 0.24$.

6 Results

6.1 Aerodynamics

The thrust generated by the SRVs obtained with LBM equals 2.2% of the propeller thrust, which follows from Fig. 6 by time-averaging and multiplying by the vane count. This value is on the lower error band of the experimentally obtained value [1]. The insufficiently resolved small scale vortices in the root region are expected to be the cause of the low SRVs' thrust. The propeller thrust and torque are unaffected by the placement of the SRVs.

The instantaneous swirl angle φ in a plane $0.4c_r$ upstream of the SRVs' LE (i.e. $x/D = 0.24$) is shown in Fig. 5. The swirl angle is defined as the angle between the tangential and axial velocity as:

$$\varphi = tan^{-1}\left(\frac{V_t}{V_a}\right) \tag{5}$$

Six regions of high swirl can be identified which are caused by the wakes behind the six propeller blades. A reduced axial velocity and increased tangential velocity are observed in the blade wakes, which increase the swirl angle. The presence of six propeller tip vortices or rotor tip vortices (RTVs) is indicated by circular regions of high swirl at the slipstream edge. As can be concluded from Fig. 4b, the tangential velocity reduces in the outboard region ($r/R > 0.8$). This causes the RTVs to have traveled a reduced circumferential distance from the propeller plane to the current plane at $x/D = 0.24$, compared to the wake flow at mid-span. Finally, four regions of high swirl can be identified at the angular locations of the SRVs. As the SRVs are lifting surfaces, an upwash is present which causes a local increase of the tangential velocity.

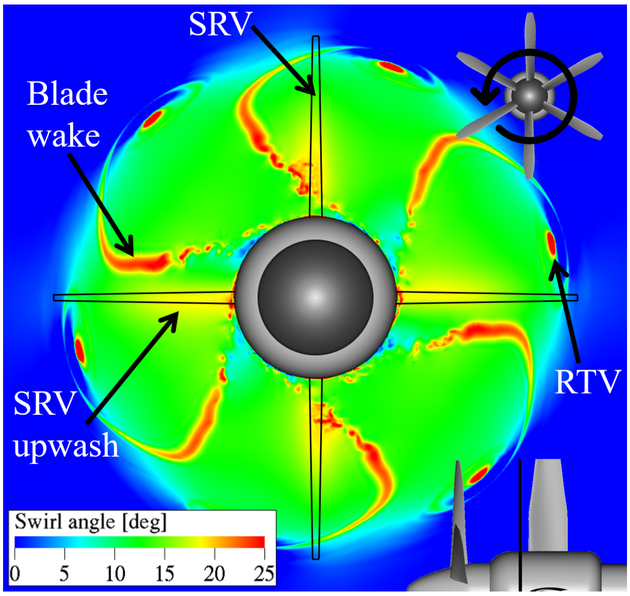

Fig. 5 : Instantaneous swirl angle φ in a plane $0.4c_r$ upstream of the SRVs (ie. $x/D = 0.24$) as indicated in the right bottom. Sources of certain phenomena are indicated. Frontview is given such that propeller rotates counterclockwise.

The swirl angle relates directly to the inflow angle of a SRV as it denotes the angle between the flow direction and a plane containing the vane. Since the patterns of high swirl presented in Fig. 5 are rotating with the tangential velocity, the SRVs encounter a varying inflow angle. The swirl angle at $r/R = 0.7$ and $0.4c_r$ upstream of the vane pointing upwards (positive y-direction) is shown with respect to phase angle in Fig. 6. Strong peaks are present of over $\varphi = 25°$ which are caused by the periodic impingement of the blade wakes as described before.

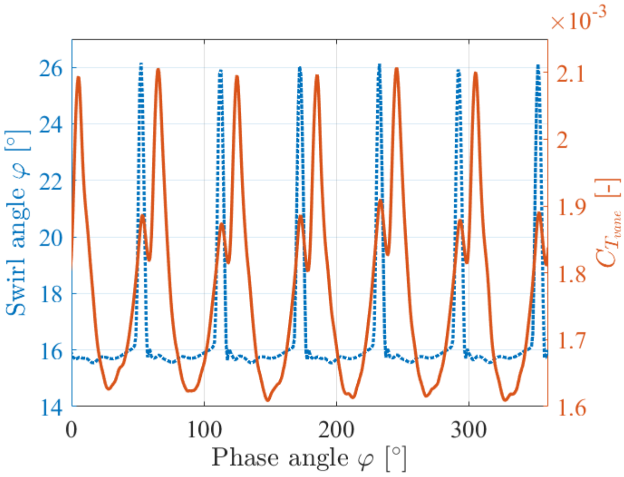

Fig. 6 : Swirl angle φ at $r/R = 0.7$ and $0.4c_r$ upstream of the upward vane indicated as a dotted line in blue. Thrust coefficient of the upward vane indicated in red.

The thrust coefficient of the upward vane $C_{T_{vane}}$ is included in Fig. 6 in red. Double peaks in thrust are present for which the first smaller peak is caused by the impingement of a RTV. The larger peak is a result of the increased swirl angle in the propeller wake of the subsequent propeller blade. The RTV impinges later than the wake of a blade as a result of the low tangential velocity at the slipstream edge. The point of maximum vane thrust is followed by a minimum which corresponds to the area of moderate swirl. Pressure plots around the surface of the vanes show that no stall is occurring, which proves the stall margin of the vanes to be sufficient.

The low-pressure cores of the RTVs are seen to effect the part of the vane where $r/R > 0.84$, which will be denoted as the tip of the vane. The instantaneous thrust generated by the tip is compared to the averaged total thrust generated by the upward vane in Fig. 7. The positive peaks in thrust overlap with the smaller peaks presented in Fig. 6 and occur when the RTV affects the front part of the vane. Negative thrust is generated by the tip when the RTV is located at the aft part. Further research on this effect is required to be able to use it for improvement of the tip shape.

On average, the tip contributes to 1.5% of the total thrust of the vane while constituting to 19% of the vane's surface area. The relatively low velocity in the outer region of the propeller slipstream is identified as the cause of the low thrust. It should be noted that the presence of the tip can still have a substantial effect on the thrust distribution of the rest of the vane.

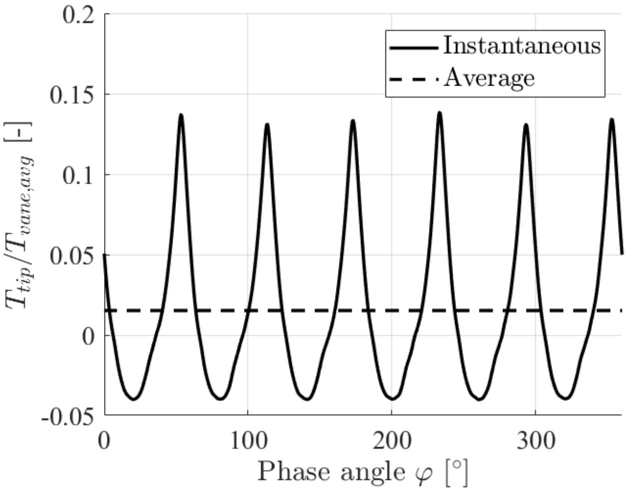

Fig. 7 : Thrust generated by the vane's tip ($r/R > 0.84$) T_{tip} normalized by the average thrust of the upward vane $T_{vane,avg}$ for one propeller rotation.

Vortex visualization is performed using the λ_2-method for which the results are presented in Fig. 8. In Fig. 8a, the rotor tip vortices (RTVs) can be seen to move inboard together with the contraction of the slipstream. In the region of $0.6 < r/R < 0.9$, no vortices are visible which indicates that the flow contains relatively low turbulence. Many small scale vortices can be identified in the region at the root ($r/R < 0.5$).

The RTVs are observed to impinge on the vanes at $r/R = 0.91$ and are then sheared in spanwise direction: the RTV at the pressure side move outboard and at the suction side inboard. When leaving the vane, the two misaligned vortices interact and start forming bridges between them, see Fig. 8b. This situation corresponds to a great extent to a configuration of a propeller in front a wing, for which this phenomenon is investigated in detail in Ref. [20].

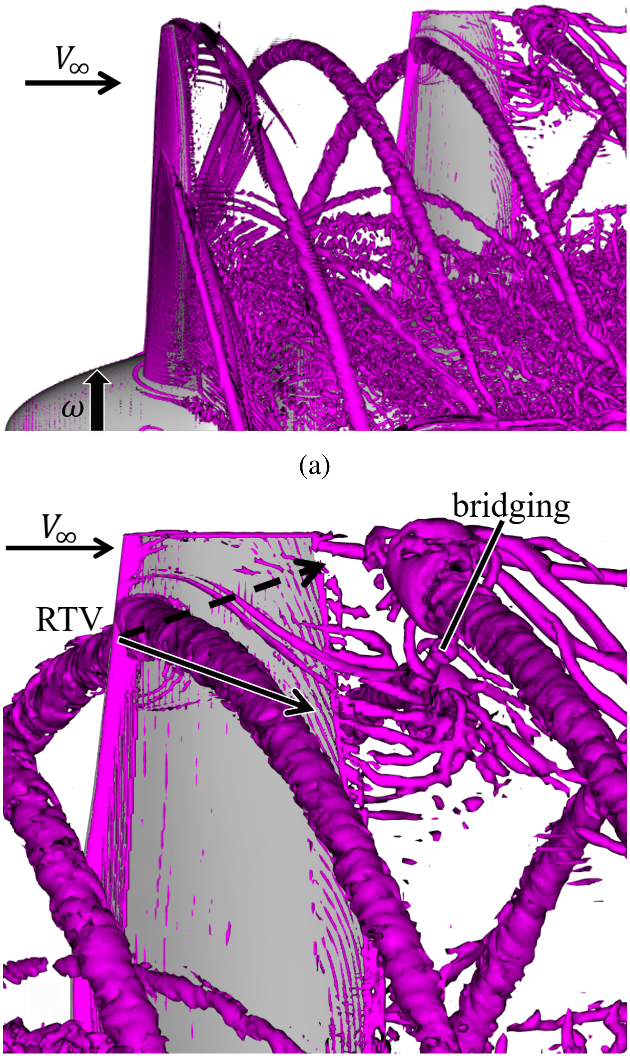

(a)

(b)

Fig. 8 : Instantaneous isosurface of $\lambda_2 = -3 \cdot 10^6$ s^{-2} in purple. (a) shows half of the geometry with the propeller rotation direction indicated by ω and the freestream velocity by V_∞. (b) shows a close-up of the pressure side of the top vane with a dashed arrow indicating the RTV direction on the pressure side and a solid arrow on the suction side.

6.2 Aeroacoustics

The aeroacoustic performance of the two configurations (with and without SRVs) is analyzed using the FW-H method as described in Sec. 3.1.2. The acoustic pressure at points on a ring with a radius of $2D$ is calculated. The ring lies in the y-plane and is centered around the midpoint between propeller and SRVs. 72 pressure traces of each 4233 samples are obtained. Welch's method [21] is applied to transform to the power spectral density (PSD) in the frequency domain. A segment length of 2048 is used as Hamming window length with 50% overlap and 8192 discrete Fourier transform points. The PSD is used to calculate the overall sound pressure level (OSPL).

In Fig. 9 the OSPL is plotted over the described ring. The blue and red lines are computed taking into account all the solid surfaces. The SRVs OFF case shows a typical noise pattern of a propeller as shown in Ref. [22]. The dashed and dotted line indicate the contribution of the propeller blades and the SRVs for the SRVs ON case, respectively.

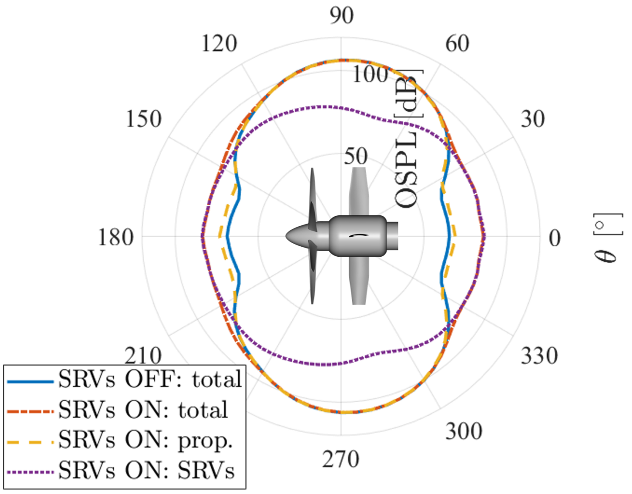

Fig. 9 : Polar plot of the overall sound pressure level (OSPL) at a distance of $2D$ from the midpoint between propeller and SRVs.

When comparing the total contributions, it can be concluded that the maximum OSPL is unaffected due to the addition of the SRVs. The contribution of the propeller is dominant in the region of maximum OSPL and overlaps to a large extend with the SRVs OFF case. The contribution of the vanes is more uniformly distributed along all directions which makes it a dominant noise source up- and downstream of the propeller. In this region, the OSPL is higher for the case with SRVs installed than for the isolated propeller.

In Fig. 10 the sound pressures are plotted in the frequency domain for three locations ($\theta = 90°$, $135°$ and $180°$) around the ring used in Fig. 9. The pressure band level (PBL) in $1/12^{th}$ octave bands is used and the frequency f is normalized by the blade passing frequency (BPF). The PBL is equal to the sound pressure level (SPL) within the specified band. At $\theta = 90°$, the isolated propeller emits mainly noise at the first harmonic ($f = \text{BPF}$). This first harmonic reduces in magnitude when moving upstream until it has completely disappeared upstream of the propeller. This is confirmed by observations in Ref. [23].

The contribution of the propeller in the SRVs ON case has a first harmonic of the same magnitude as the isolated propeller. The propeller does however get effected by the presence of the SRVs, as can be concluded from the emitted noise at the higher harmonics (multiples of the BPF). This becomes especially apparent at $\theta = 135°$. The unsteady loading of the SRVs causes a varying potential field which propagates upstream and effects the blades of the propeller [24]. This alters the loading of the propeller and results in this higher-harmonics noise.

The vanes are the cause of considerable noise at the higher harmonics. As shown in the polar plot of the OSPL, this noise is more uniformly distributed along all directions, which results in PBL peaks of roughly the same magnitude for the three locations displayed in Fig. 10. Due to the dominance of the first harmonic at $\theta = 90°$, the contribution of the vanes to the OSPL is minimal at this location. As the first harmonic caused by the blades reduces when moving upstream, the higher harmonics caused by the SRVs become dominant.

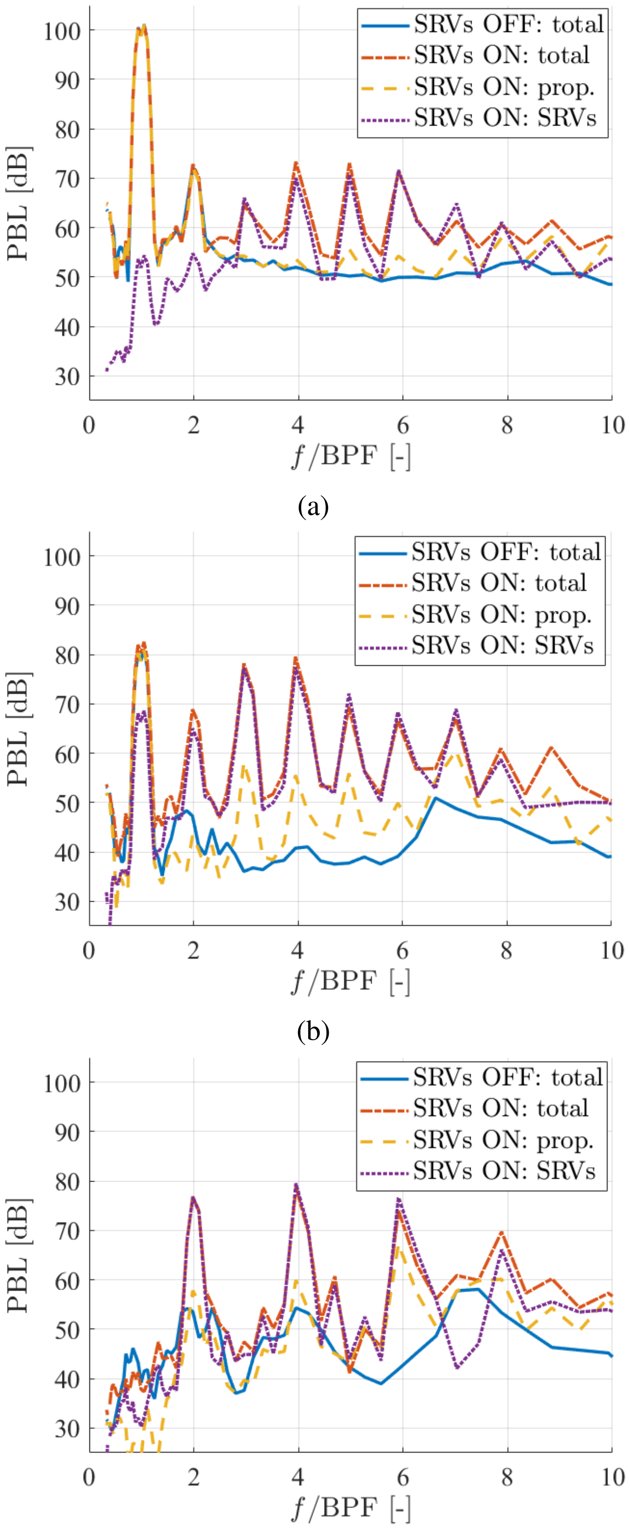

(a)

(b)

(c)

Fig. 10 : Pressure band level (PBL) in $1/12^{th}$ octave bands at a distance of $2D$ from the midpoint between propeller and SRVs at (a) $\theta = 90°$, (b) $\theta = 135°$ and (c) $\theta = 180°$.

It is expected from Ref. [4] that the impingement of the RTVs on the SRVs is an additional noise source. To investigate this assumption, the vanes are split up into four surfaces: LE, TE, tip ($r/R > 0.84$) and middle. The former three surfaces are used to define VR12 as described in 3.1.3. The contribution of each of these four surfaces to the OSPL is shown in Fig. 11. The leading edge (LE) is the main source of noise with an OSPL of 1.4 to 6.6 dB higher than the contribution of the tip. Further research into a configuration where the length of the vanes is reduced could confirm to what extent the expected noise reduction is present.

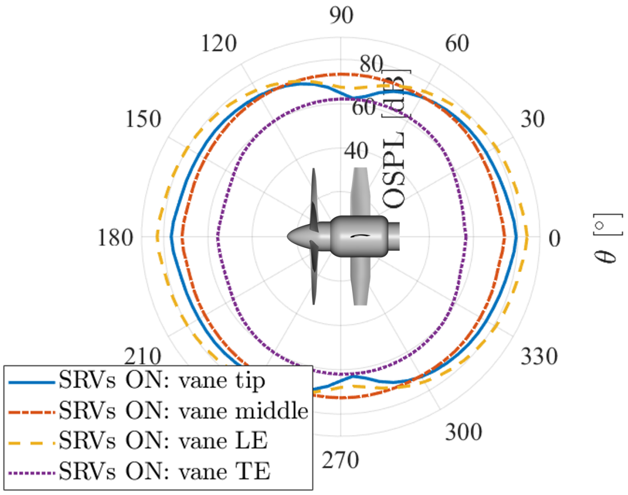

Fig. 11 : Polar plot of the overall sound pressure level (OSPL) at a distance of $2D$ from the midpoint between propeller and SRVs.

7 Conclusion

An aerodynamic and aeroacoustic study on the effect of the swirl recovery vanes behind a propeller are presented in this paper. A numerical study has shown that the SRVs' inflow fluctuates due to blade wakes and tip vortices present in the propeller slipstream, resulting in two distinct peaks in vane thrust. Additionally, the tip regions of the SRVs are shown to produce only 1.5% of the total vane thrust, while constituting to 19% of the SRVs' surface area. Further research should point out whether the tip shape can be altered to take advantage of the tip vortex impingement.

The maximum sound pressure level is found to be unaffected by the placement of the vanes, whereas the noise is increased up- and downstream of the propeller. The propeller blades have a low contribution to the overall noise in these regions such that the vanes have a dominant effect. Besides, the frequency of the sound is increased as the SRVs emit tonal noise at harmonics of the BPF. Simulations on a configuration with shorter vanes are required to quantify the noise benefit of avoiding the propeller tip vortex impingement.

References

[1] Li Q, Öztürk K, Sinnige T, Ragni D, Eitelberg G, Veldhuis LLM and Wang Y. Design and experimental validation of swirl recovery vanes for propeller propulsion systems. *35th AIAA Applied Aerodynamics Conference*, Denver, Colorado, AIAA 2017-3571, 2017.

[2] Wang Y, Li Q, Eitelberg G, Veldhuis LLM and Kotsonis M. Design and numerical investigation of swirl recovery vanes for the Fokker 29 propeller. *Chinese Journal of Aeronautics*, Vol. 27, No. 5, pp 1128-1136, 2014.

[3] Dittmar JH and Hall GH. The effect of swirl recovery vanes on the cruise noise of an advanced propeller. *13th Aeroacoustics Conference*, Reston, Virigina, AIAA-90-3932, 1990.

[4] Sinnige T, Van Kuijk JJA, Lynch KP, Ragni D, Eitelberg G and Veldhuis LLM. The effects of swirl recovery vanes on single-rotation propeller aerodynamics and aeroacoustics. *21st AIAA/CEAS Aeroacoustics Conference*, Reston, Virginia, AIAA 2015-2358, 2015.

[5] Brandt J and Selig M. Propeller Performance Data at Low Reynolds Numbers. *49th AIAA Aerospace Sciences Meeting including the New Horizons Forum and Aerospace Exposition*, Reston, Virigina, AIAA 2011-1255, 2011.

[6] Avallone F, Casalino D and Ragni D. Impingement of a propeller-slipstream on a leading edge with a flow-permeable insert: a computational aeroacoustic study. *International Journal of Aeroacoustics*, (in press).

[7] Casalino D, Hazir A and Mann A. Turbofan broadband noise prediction using the lattice

Boltzmann method. *AIAA Journal*, Vol. 56, No. 2, pp 609-628, 2018.

[8] Pérot F, Moreau S, Kim M-S, Henner M and Neal D. Direct aeroacoustics predictions of a low speed axial fan. *16th AIAA/CEAS Aeroacoustics Conference*, Stockholm, Sweden, AIAA 2010-3887, 2010.

[9] Krüger T, Kusumaatmaja H, Kuzmin A, Shardt O, Silva G and Viggen EM. *The lattice Boltzmann method*. 1st edition, Springer International Publishing, 2017.

[10] Chen H, Chen S and Matthaeus WH. Recovery of the Navier-Stokes equations using a lattice-gas Boltzmann method. *Physical Review A*, Vol. 45, No. 8, pp 5339-5342, 1992.

[11] Bhatnagar PL, Gross EP and Krook M. A model for collision processes in gases. I. Small amplitude processes in charged and neutral one-component systems. *Physical Review*, Vol. 94, No. 3, pp 511-525, 1954.

[12] Yakhot V and Orszag SA. Renormalization group analysis of turbulence. I. Basic theory. *Journal of Scientific Computing*, Vol. 1, No. 1, pp 3-51, 1986.

[13] Teixeria CM. Incorporating turbulence model into the lattice-Boltzmann method. *International Journal of Modern Physics C*, Vol. 9, No. 8, pp 1159-1175, 1998.

[14] Wilcox DC. *Turbulence modeling for CFD*. 3rd edition, DCW Industries Inc., 2006.

[15] Bres GA, Perot F and Freed D. Properties of the lattice-Boltzmann method for acoustics. *15th AIAA/CEAS Aeroacoustic Conference*, Miami, Florida, AIAA 2009-3395, 2009.

[16] Ffowcs Williams, JE and Hawkings DL. Sound generation by turbulence and surfaces in arbitrary motion. *Philosophical Transactions of the Royal Society of London. Series A, Mathematical and Physical Sciences*, Vol. 264, No. 1151, pp 321-342, 1969.

[17] Farassat F and Succi GP. A review of propeller discrete frequency noise prediction technology with emphasis on two current methods for time domain calculations. *Journal of Sound and Vibration*, Vol. 71, No. 3, pp 399-419, 1980.

[18] Casalino D. An advanced time approach for acoustic analogy predictions. *Journal of Sound and Vibration*, Vol. 261, No. 4, pp 583-612, 2003.

[19] Curle N. The influence of solid boundaries upon aerodynamic sound. *Proceedings of the Royal Society of London. Series A, Mathematical and Physical Sciences*, Vol. 231, No. 1187, pp 505-514, 1955.

[20] Johnston RT and Sullivan JP. Unsteady wing surface pressures in the wake of a propeller. *Journal of Aircraft*, Vol. 30, No. 5, pp 644-651, 1993.

[21] Welch P. The use of fast Fourier transform for the estimation of power spectra: a method based on time averaging over short, modified periodograms. *IEEE Transactions on Audio and Electroacoustics*, Vol. 15, No. 2, pp 70-73, 1967.

[22] Marte JE and Kurtz DW. A review of aerodynamic noise from propellers, rotors, and lift fans. *NASA Technical Report 32-1462*, 1970.

[23] Deming AF. Propeller rotation noise due to torque and thrust. *The Journal of the Acoustical Society of America*, Vol. 12, No. 1, pp 173-182, 1940.

[24] Li Q, Wang Y and Eitelberg G. An investigation of tip vortices unsteady interaction for Fokker 29 propeller with swirl recovery vane. *Chinese Journal of Aeronautics*, Vol. 29, No. 1, pp 117-128, 2016.

Copyright Statement